

A high resolution comparative study of the slowly contracting, starless cores, L694-2 and L1544

Jonathan P. Williams

Institute for Astronomy, 2680 Woodlawn Drive, Honolulu, HI 96822; jpw@ifa.hawaii.edu

and

Philip C. Myers

Harvard-Smithsonian Center for Astrophysics, 60 Garden Street, Cambridge, MA 02138; pmyers@cfa.harvard.edu

ABSTRACT

We present interferometric observations of $\text{N}_2\text{H}^+(1-0)$ in the starless, dense core L694-2 and compare them to previously published maps of L1544. Both cores are starless, centrally condensed, and show spectral signatures of rotation and collapse. We fit radially averaged spectra using a two-layer infall model and measure the variation of opacity and infall speed in each core. Both functions increase toward the center of each core but the radial gradients are shallower, and the central values lower, in L694-2. This general behavior is predicted in models of gravitational collapse with thermal plus magnetic support and the lower values in L694-2 may be due to its lower mass or a slightly earlier evolutionary state. In either case, it appears that both cores will form stars within a few 10^4 yr.

Subject headings: ISM: individual(L694, L1544) — ISM: kinematics and dynamics — stars: formation

1. Introduction

Low mass stars form via the gravitational collapse of “dense cores” with densities $n(\text{H}_2) > 10^4 \text{ cm}^{-3}$ which are built up either via the diffusion of neutrals past ions tied to magnetic field lines or the dissipation of turbulent support (Evans 1999). The Lynds catalog (Lynds 1962) of optically selected dark cores provides an excellent starting point for the observational study of the processes involved. Lynds cores are generally compact, dense and emit strongly in a wide range of molecular lines and continuum at millimeter wavelengths. This allows for detailed investigations of their dynamics and comparison with theoretical models (e.g. Gueth et al. 1997).

The first stage in star formation, the collapse of a starless core, can be diagnosed through the analysis of self-absorbed spectral features (Leung & Brown 1977). For sufficiently high optical depth and a decreasing excitation temperature with radius, the outer part of a core absorbs the emission from the center. The resulting spectral profile will show a dip near the velocity of the absorbing layer. If the core is collapsing, this dip will appear at higher velocities than the bulk of the core emission. Such red-shifted self-absorption is the principal signature of inward motions. Probably because self-absorption requires a fairly well-tuned combination of optical depth and excitation conditions, however, the window of observability of infall in starless cores is fairly short (e.g. Gregersen & Evans 2000).

L1544 is the prototypical example of a collapsing starless core. It shows strong red-shifted self-absorption in a number of molecular species (e.g., Tafalla et al. 1998; Caselli et al. 2002). These have been interpreted to show both rotation and collapse (Ohashi et al. 1999) and the infall motions have been compared in detail with a variety of collapse models, ranging from gravitational free-fall (Whitworth & Ward-Thompson 2001), ambipolar diffusion (Ciolek & Basu 2000), external compression (Hennebelle et al. 2003), and turbulent cooling (Myers & Lazarian 1998). L1544 has received so much attention as it shows the most clearly defined infall signatures of any starless core. It is important, nevertheless, to study other cores to constrain the models further.

L694-2 was identified as a collapsing, starless core by Lee and collaborators; Lee & Myers (1999) used the Digital Sky Survey to define the optical properties of the most opaque Lynds cores in detail and followed up with a molecular line survey of those that were determined to be starless (Lee, Myers, & Tafalla 1999). L694-2 came to prominence in this work as a “strong infall candidate” on the basis of pronounced red-shifted self-absorption in the CS(2–1) line. Subsequently Lee, Myers, & Plume (2004) showed similar infall profiles in CS(3–2) and DCO⁺(2–1). Their spectral fits indicated that the infall speed increased with optical depth and, presumably therefore, toward the center of the core.

The starless nature of L694-2 was deduced from the lack of an IRAS point source and confirmed by a VLA non-detection at 3.6 cm (Harvey et al. 2002). Together these limit the luminosity of an embedded source to $L \lesssim 0.3 L_{\odot}$. Subsequent millimeter continuum observations by Harvey et al. (2003a) showed that there was no compact, disk-like source to a sensitivity $M_{disk} \lesssim 5 \times 10^{-4} M_{\odot}$. The core is included in the “c2d” Spitzer Legacy program which will show whether a very low luminosity source exists (Evans et al. 2003)

L694-2 also has similar structural and chemical properties as L1544 (Crapsi et al. 2005). The low temperatures and high densities of starless cores result in substantial molecular depletion onto grain surfaces (Tafalla et al. 2002). These chemical properties imply that to follow the dynamics toward the core centers requires a relatively inert molecular probe

that remains in the gas phase. To measure relative (infall) motions, in particular, requires high optical depth and therefore high abundance. Only a handful of molecules meet these conditions.

N_2H^+ is well suited as a relatively abundant species in starless cores that suffers little depletion except at the very highest column densities (Bergin et al. 2002). Tafalla et al. (1998) found that the $J = 1 - 0$ line was double-peaked due to self-absorption at the center of L1544. Williams et al. (1999; hereafter Paper I) subsequently mapped this line at $10''$ resolution to examine the velocity field at scales approaching that of a protostellar disk (1000 AU). In that work, we found a centrally condensed, slightly elongated core, and an increasing infall velocity toward the center.

Lee, Myers & Tafalla (2001) mapped $\text{N}_2\text{H}^+(1-0)$ emission in L694-2 at $50''$ resolution and found a compact, centrally condensed core. Here, we present combined interferometric plus singledish observations of N_2H^+ in L694-2 at $10''$ resolution. Although the N_2H^+ spectra do not split into two distinct peaks as in L1544, they do have identifiable “red shoulders” due to self-absorption that are equally indicative of collapse. We compare the two datasets and model the spectra in both cores using new analytic tools made available by De Vries & Myers (2005).

The observations are presented in §2, and the results and modeling in §3. We show that L1544 is more centrally condensed and has a higher infall speed and gradient than L694-2. This general trend is discussed in the context of gravitational collapse models in §4. Throughout the paper, we adopt a distance to L694-2 of 230 pc based on optical star counts by Kawamura et al. (2001) and 140 pc for L1544 based on its association with the Taurus cloud (Elias 1978).

2. Observations

L694-2 was observed with the 10 element Berkeley-Illinois-Maryland array¹ in its compact C configuration on 1999, June 7, 8 and 11. The phase center of the observations was $\alpha(2000) = 19^{\text{h}}41^{\text{m}}04^{\text{s}}.5$, $\delta(2000) = 10^{\circ}57'02''$ and the total (on-source) integration time was 14 hours. The amplitude and phase calibration was performed from 3 minute integrations of the quasar 1925+211 interleaved with each 22 minute observation on source. The passband and flux calibration was carried out from a 30 minute observation of Uranus toward the end of each track. The derived flux for 1925+211 was 1.7 Jy.

¹The BIMA array is operated with support from the National Science Foundation under grants AST-9981308 to UC Berkeley, AST-9981363 to U. Illinois, and AST-9981289 to U. Maryland.

The digital correlator was configured with 512 channel windows at a bandwidth of 6.25 MHz (0.04 km s⁻¹ velocity resolution per channel) centered on the 7 hyperfine components of N₂H⁺(1–0) in the lower sideband and C³⁴S(2–1) in the upper sideband. Eight 32 channel windows at a bandwidth of 100 MHz. were used to measure continuum radiation. Data were reduced with the MIRIAD package using standard procedures. The data sets from each day were calibrated separately and then transformed together with natural weighting. The resulting beamsize was 9''.5 × 7''.1.

The N₂H⁺ lines were detected with a high signal-to-noise ratio in the lower sideband, but no emission was detected in the upper sideband, implying a 3σ upper limit of 1.5 K km s⁻¹ for the C³⁴S emission integrated over velocities 9.3 – 9.9 km s⁻¹. No continuum emission was detected at a 3σ level of 2.1 mJy beam⁻¹.

The projected baselines of the interferometer data ranged from 1.9 to 27 kλ. To provide information at lower spatial frequencies, we observed L694-2 using the Five College Radio Astronomy Observatory 14 m telescope (FCRAO²) on 1999 December 20. We used the 16 element, focal plane array SEQUOIA and a system of autocorrelation spectrometers at a spectral resolution of 20 kHz. Standard position-switching procedures were used and resulted in a Nyquist sampled map with an rms noise of 0.05 K per 0.06 km s⁻¹ channel. Antenna temperatures were multiplied by a gain of 43.7 Jy K⁻¹ to convert to flux units and the singledish data were then added to the interferometer data using the combination method described in Stanimirovic et al. (1999). The analysis in this paper was performed on the combined BIMA+FCRAO dataset convolved to a spatial resolution of 10'' and interpolated to velocity channels of width 0.05 km s⁻¹.

L1544 had been previously observed in a similar way with the BIMA array and IRAM 30 m antenna (Paper I). To make an unbiased comparison between the two cores, we re-reduced the data and combined the interferometer and singledish datasets using the same linear combination technique described above.

3. Results

3.1. Spectral comparison

The $J = 1 - 0$ transition of N₂H⁺ has 7 hyperfine components, two groups of three and one isolated (Caselli, Myers & Thaddeus 1995). The linewidths of L694-2 and L1544 are

²FCRAO is supported in part by the National Science Foundation under grant AST-0100793 and is operated with permission of the Metropolitan District Commission, Commonwealth of Massachusetts

similar and sufficiently small that all 7 components can be distinguished. Figure 1 shows three different hyperfine components, ordered from high to low optical depth, toward the two cores. The L1544 data have been smoothed to $16''$ to achieve the same linear resolution, 2300 AU, as the L694 data. In each case, the spectra are most asymmetric in the top panel and become more symmetric as the optical depth of the hyperfine component decreases in the middle and bottom panels. The asymmetries must be due, therefore, to radiative transfer effects rather than kinematics. We conclude that both cores exhibit red-shifted self-absorption. This is strong evidence for core collapse.

The self-absorption features are less pronounced in the L694-2 spectra, which show shoulders, than in the L1544 spectra, which show dips. This is indicative of a lower opacity and is in agreement with the multi-transition analysis by Crapsi et al. (2005) who found that the N_2H^+ column density is $\sim 25 - 30\%$ lower in L694-2 than in L1544.

The isolated component, $F_1F = 10 - 11$, has the lowest optical depth and therefore is the weakest and most symmetric. Although we were able to analyze the dynamics using this line in L1544 in Paper I, the lower optical depth and signal-to-noise ratio precludes a similar study of the L694-2 dataset. We therefore focus the remainder of the analysis and comparison of the two cores on the central $F_1F = 23 - 12$ component at 93.1737767 GHz, as it is the brightest and has the highest optical depth, making it the most sensitive for tracing relative motions in the core.

3.2. Moment maps

Maps of the first two moments of the $F_1F = 23 - 12$ hyperfine component are plotted in Figures 2 (L694-2) and 3 (L1544). The contours of zeroth moment, or integrated intensity, are similar to dust continuum images (Visser et al. 2002; Ward-Thompson, Motte, & André 1999) suggesting that there is negligible N_2H^+ depletion in each core and that this transition is a reliable tracer of the dynamics toward the core centers at ~ 2000 AU resolution scales.

The first moment, or mean velocity, of the line is overlaid in color scale over the integrated intensity contours. In L694-2, there is a central low velocity (blue) hole surrounded, almost in a complete ring, by higher velocities. In L1544, there is a clear trend of low to high (red) velocities across the core, but the lines of constant velocity are curved in a ‘C’-shape. In each case, the velocity pattern cannot be explained solely by rotation or shear across the core. Rather, following the earlier work by Tafalla et al. (1998) in L1544 and Lee et al. (1999) in L692-2, we suggest that the N_2H^+ velocity pattern can be explained by a combination of rotation and core contraction.

The spectroscopic signature of core collapse is red-shifted self-absorption. The mean

velocity of such spectra is lower than in the absence of self-absorption or infall and therefore appears in a first moment map as a dip toward low, or blue, velocities. Core rotation manifests itself as an one-dimensional gradient in the first moment map, however, and the two effects can therefore be distinguished (Adelson & Leung 1988). Walker, Narayanan, & Boss (1994) modeled the radiative transfer of collapsing, rotating cores and coined the phrase “blue-bulge” to describe the feature in the mean velocity field where infall motions dominate over rotation. For a centrally condensed core with uniform rotation and increasing infall speed toward the center, the contours of constant velocity form a ‘C’-shape near the peak of emission, dependent on the inclination of the rotation axis to the line of sight. They point out that this feature is a more robust signature of infall than the classic line asymmetry and subsequently demonstrate its applicability in two star-forming systems (Narayan, Walker, & Buckley 1998; Narayan et al. 2002).

The mean velocity maps of both L694-2 and L1544 also show the “blue-bulge” signature of collapse superimposed on rotation. A central blue dip can be clearly seen toward the center of L694-2. The velocity gradient is higher in L1544 so the lines of constant velocity do not wrap onto themselves but nevertheless are clearly curved. Using these maps, we are able to follow the core dynamics beyond the center where the spectral asymmetries in Figure 1 are most clear.

To isolate and analyze the infall motions, we removed the rotation in each core by subtracting a linear velocity gradient from the maps. This is an approximation as the N_2H^+ line is optically thick and self-absorbed. We define the best fit, however, by minimizing the dispersion in mean velocity within the central $40''$, and it is weighted (simply by the number of pixels) to the outer parts of the core where the optical depth is low. Therefore, the error in measuring the rotation is likely to be small. The subtracted mean velocity image are shown for L694-2 and L1544 in the right panels of Figures 2 and 3 respectively. The magnitude and direction of the rotation vector is shown in the bottom right corner. The velocity gradient in L1544, 4.1 km s^{-1} , is similar to the value determined in Paper I from a different modeling technique. The gradient in L694-2 is much smaller, 0.5 km s^{-1} . Without knowledge of the core geometries and inclination of the rotation axes, however, it is not possible to compare their angular momenta directly.

In both cores, the residual (mean minus rotation) velocity field shows a marked bipolar deviation from circular symmetry. The signal-to-noise ratios of the data are unfortunately too low to study this quantitatively but it is perhaps noteworthy that the bipolarity is not aligned with the direction of core elongation. This suggests that the infall speed is not spherically symmetric, as would be expected for a purely gravitational flow resisted by isotropic pressure.

The high velocity gradient in L1544 stretches the color scale and masks the central blue-bulge feature in the residual map. The increase in the residual velocity field away from the core center is shown for both cores in Figure 4 and demonstrates that the bluebulge dip is steeper in L1544 than L694-2. This could be due to either or both a steeper radial variation of opacity and infall speed. To examine this further we return to an examination of the spectral profiles.

3.3. Infall modeling

By removing the velocity field due to rotation, we can isolate the infall dynamics in each core. Away from the center, however, the signal-to-noise ratios are too low to allow modeling of individual spectra and we binned the data into concentric radial annuli with $10''$ width. This allows us to measure the radial variations of optical depth and infall speed. The radial averaging is justified in L694-2 by the approximate circular symmetry of the core and the analysis by Harvey et al. (2003a, 2003b) who showed that the core density profile can be fit either by a spherically symmetric model or a cylinder that is nearly pole on. Harvey et al. (2003b) also noted that a cylindrical configuration would be prone to collapse. L1544 is more elongated but we found an approximately circular distribution of infall speed in Paper I.

The average spectra for the two cores are shown as histograms in Figure 5. The systemic motion of each core (defined from the fits described below) is shown as a dotted vertical line. Moving out from the core centers (top panels) to the outer parts (lower panels), the spectra in both cores become weaker, more symmetric, and their mean velocity shifts to higher values. This behavior can be explained by an absorbing layer of gas falling onto the core. At small radii, the optical depths are high and the profiles show relatively strong self-absorption. Because the absorbing layer is falling onto the core, the absorption is redshifted with respect to our line of sight and the profiles therefore appear asymmetric. As the optical depth decreases at larger radii, there is less self-absorption and the spectra become more symmetric.

The values of the optical depth and infall speed can be determined via detailed modeling. We were able to produce very good fits to the radially averaged spectra using the two layer infall model described in Myers et al. (1995) and the parameter search technique of De Vries & Myers (2005). Following the recommendation in that paper, we used the `hi115` De Vries & Myers model. The `hi115` analytic models are characterized by 5 parameters: the systemic velocity, velocity dispersion, total optical depth, peak temperature, and the infall speed; v_{LSR} , σ , τ , T_{peak} , and v_{in} respectively. The infall speed is defined such that the front layer moves at velocity $v_{LSR} + v_{in}$ with respect to the observer and the rear layer at velocity

$v_{LSR} - v_{in}$. Measurement of the infall speed requires a sufficiently high opacity to create significant self-absorption in the spectra, and was not possible in the outer parts of each core. The fits are only shown, therefore, for the spectra where the modeled optical depth is greater than unity; $\theta < 30''$ for L694-2 and $\theta < 40''$ for L1544. The model spectra are overlaid as solid lines over the histograms in Figure 5 and the parameters that define them are listed in Table 1.

The parameter uncertainties were estimated by taking the best fit models in Table 1, adding random noise with the same rms as the observed noise, and re-fitting using the same procedure. The error in each parameter was set equal to the dispersion in the fits over 50 repeats of this process. We found that the errors in v_{LSR} , σ , and T_{peak} were negligible, but the errors in τ and v_{in} , whose value depends on relatively subtle features in the spectral profiles, were larger and ranged from $\sim 5 - 15\%$.

The radial variations of modeled optical depth and infall speed are shown in Figure 6. Within the $\sim 0.01 \text{ km s}^{-1}$ uncertainties, the analysis here indicates similar, but slightly higher, infall velocities in L1544 than those measured in Paper I using a different fitting method to the isolated hyperfine component. We can be more confident of the relative differences between L1544 and L694-2, however, because we have applied an identical analysis to observations of the same hyperfine component. We find that both the optical depth and infall speed are higher in the central 3500 AU in L1544 than in L694-2 and both decline more steeply with radius. The higher opacity was immediately apparent from the stronger self-absorption features in the spectra in Figure 1. The rapid decline toward larger radii reflects the steeper blue-bulge signature seen in Figure 4.

4. Discussion and Conclusions

We have compared similar maps of the $J = 1 - 0$ transition of N_2H^+ in two collapsing, starless cores, L694-2 and L1544. Toward the core centers, the hyperfine components show an increasing asymmetry with optical depth. This is strong evidence for inward motions and complements earlier studies of collapse at larger scales by Lee et al. (2001) in L694-2 and Tafalla et al. (1998) in L1544, using lower resolution observations of CS.

We then analyzed the dynamical structure of the cores in more detail by examining the moment maps of the most optically thick, $F_1F = 23 - 12$ hyperfine component. The mean velocity pattern showed a systematic variation across the cores from rotation and an additional “bluebulge” toward the center from infall. This follows earlier modeling work and observations of other star forming regions by Walker et al. (1994) and Narayanan (1997). By removing the velocity gradient from the data, we were able to isolate the blueward shift due

to infall asymmetry. The depth of the bluebulge is similar, $\sim 0.05 \text{ km s}^{-1}$, in both cores but the size of the dip is larger in L694-2 reflecting a shallower opacity gradient. These velocity-shifted spectra were then radially averaged and modeled using an automated parameter search technique by De Vries & Myers (2005) applied to the two-layer infall model of Myers et al. (1995).

The spectral fits show that both cores have low velocity dispersions, $\sigma \sim 0.08 \text{ km s}^{-1} = 1.5\sigma_T(\text{N}_2\text{H}^+)$, for a kinetic temperature $T_K = 10 \text{ K}$. The non-thermal motions are therefore very small, $\sigma_{NT}/\sigma_T(\text{H}_2) \simeq 1/3$. In fact, much of the non-thermal motion may be due to infall itself. Whether this is the case or not, the pressure support in the cores, which is proportional to the square of the velocity dispersion, is predominantly thermal. The turbulence that is seen at larger scales has almost completely dissipated and the infall motions that we have measured here can constrain theoretical models of the gravitational flows in a core supported by a thermal, or thermal plus magnetic, pressure (e.g. Shu 1977; Mouschovias 1976).

Indeed the variation of infall speed with radius in L1544 has been successfully reproduced using an ambipolar diffusion model by Ciolek & Basu (2000) and the free-fall collapse of a sphere with Plummer-like density profile by Whitworth & Ward-Thompson (2001). These two models differ in that the total star formation timescale is very different, $t_{\text{sf}} = 2.7 \text{ Myr}$ for ambipolar diffusion, compared to $t_{\text{sf}} = 0.04 \text{ Myr}$ for the free-fall collapse timescale of the central flat region of the Plummer core. They agree, however, in how far L1544 is from the end of this process. Ambipolar diffusion lengthens the build-up of a core to a critical state where magnetically diluted collapse takes place and observable infall motions only occur in the last few percent of t_{sf} . The best fit Ciolek & Basu model places the age of L1544 at $t \simeq 0.99t_{\text{sf}}$, or only $3 \times 10^4 \text{ yr}$ from forming a star. Whitworth & Ward-Thompson (2001) place the age of L1544 of about 50% of the central free-fall timescale so only $2 \times 10^4 \text{ yr}$ from star formation. Myers (2005) also predicts a similar late stage of collapse for L1544 in a purely gravitational collapse model applied to different geometries.

A general feature of both models (and indeed any model of gravitational collapse) is that the infall speed increases with time *at all radii*. The central density also increases, although the density profile in the outer parts, radii $\gtrsim 2000 \text{ AU}$, is independent of time. At the resolution of these observations, the density profiles of the two cores should therefore appear very similar but the central column density should be higher in the more evolved core and the infall speeds should be higher throughout.

The main results of the spectral fitting are the radial variations of infall speed and opacity in the two cores (Table 1 and Figure 6). In the inner regions, $r < 3500 \text{ AU}$, L1544 is $\sim 25\%$ more opaque and collapsing about $\sim 15\%$ faster. This may indicate that L694-2 is somewhat less evolved toward star formation than L1544, but it may also be due to its lower

mass. The precise masses of the cores depend on how their outer boundaries are defined, but within the $\sim 10^4$ AU size of our N_2H^+ maps, we estimate a mass $\sim 1 M_\odot$ for L694-2 from Visser et al. (2002) and $\sim 1.5 M_\odot$ for L1544 from Ward-Thompson et al. (1999). Whether evolution or mass explains the differences in the model fits, the centrally concentrated blue-bulge signatures of collapse are remarkably similar and indicate that point mass formation at the centers of *both* cores will occur in a few 10^4 yr.

We caution that the observed values of the radii in the plot of infall speed (Figure 6) do not directly translate to physical core radii because the spectral features essentially convolve the emission from several distinct regions along the line of sight. A quantitative comparison with theory requires calculating the radiative transfer of dynamical models (e.g. Choi et al. 1995). This is also necessary to tie the N_2H^+ observations presented here to measurements of infall at large scales from CS observations (Lee et al. 2001; Tafalla et al. 1998). This adds the significant additional complexity of core chemistry. The relevant chemical timescales for molecule formation and depletion are similar to the dynamical timescales of collapse. Consequently, the comparison of infall motions measured in two different molecular species requires combined modeling of structure, dynamics, chemistry, and radiative transfer (e.g. Doty, Schöier, & van Dishoeck 2004).

Due to the relatively low signal-to-noise ratio of these data and the subtle self-absorption features in the spectra, we have only been able to examine the radial variation of core properties. The residual moment maps, after subtraction of a velocity gradient, show additional structure. These approximately bipolar velocity features are not aligned with the elongation of the cores, measured from the central intensity contours of L694-2 and L1544. Optical depth effects alone, therefore, are not the sole explanation and it appears that the infall speed is not spherically symmetric. Both core elongation and a preferred direction for collapse are expected from a static magnetic field geometry. A quantitative investigation of the two-dimensional density and velocity structure requires more sophisticated radiative transfer models (e.g. Hogerheijde, & van der Tak 2000) and higher quality data, such as will soon be available with the CARMA array (Woody et al. 2004).

Several other starless collapsing core candidates are known. It will be very worthwhile to study them at high resolution in molecular species that probe the dynamics at their centers. The comparison of such data will give further insight into the processes that collapse the dense ISM down to planetary disk scales.

We thank Chris De Vries for advice concerning his code to fit the spectra. We acknowledge support from NSF grant AST-0324328 (JPW) and NASA Origins of Solar Systems grant NAG5-13050 (PCM).

5. References

- Adelson, L. M., & Leung, C. M. 1988, *MNRAS*, 235, 349
- Bergin, E. A., Alves, J., Huard, T., & Lada, C. J. 2002, *ApJ*, 570, L101
- Caselli, P., Walmsley, C. M., Zucconi, A., Tafalla, M., Dore, L., & Myers, P. C. 2002, *ApJ*, 565, 331
- Caselli, P., Myers P.C., & Thaddeus, P. 1995, *ApJ*, 455, L77
- Choi, M., Evans, N. J., Gregersen, E. M., & Wang, Y. 1995, *ApJ*, 448, 742
- Ciolek, G. E., & Basu, S. 2000, *ApJ*, 529, 925
- Crapsi, A., Caselli, P., Walmsley, C. M., Myers, P. C., Tafalla, M., Lee, C. W., & Bourke, T. L. 2005, *ApJ*, 619, 379
- De Vries, C. H., & Myers, P. C. 2005, *ApJ*, 620, 800
- Doty, S. D., Schöier, F. L., & van Dishoeck, E. F. 2004, *A&A*, 418, 1021
- Elias, J. H. 1978, *ApJ*, 224, 857
- Evans, N. J. et al. 2003, *PASP*, 115, 965
- Evans, N. J. 1999, *ARAA*, 37, 311
- Gregersen, E. M., & Evans, N. J. 2000, *ApJ*, 538, 260
- Gueth, F., Guilloteau, S., Dutrey, A., & Bachiller, R. 1997, *A&A*, 323, 943
- Harvey, D. W. A., Wilner, D. J., Di Francesco, J., Lee, C. W., Myers, P. C. & Williams, J. P. 2002, *AJ*, 123, 3325
- Harvey, D. W. A., Wilner, D. J., Myers, P. C., & Tafalla, M. 2003a, *ApJ*, 597, 424
- Harvey, D. W. A., Wilner, D. J., Lada, C. J., Myers, P. C., & Alves, J. F. 2003b, *ApJ*, 598, 1112
- Hennebelle, P., Whitworth, A. P., Gladwin, P. P., & André, P. 2003, *MNRAS*, 340, 870
- Hogerheijde, M. R., & van der Tak, F. F. S. 2000, *A&A*, 362, 697
- Leung, C. M., & Brown, R. L. 1977, *ApJ*, 214, L73
- Kawamura, A., Kun, M., Onishi, T., Vavrek, R., Domsa, I., Mizuno, A., & Fukui, Y. 2001, *PASJ*, 53, 1097
- Lee, C. W., & Myers, P. C. 1999, *ApJS*, 123, 233
- Lee, C. W., Myers, P. C., & Tafalla, M. 1999, *ApJ*, 526, 788
- Lee, C. W., Myers, P. C., & Tafalla, M. 2001, *ApJS*, 136, 703
- Lee, C. W., Myers, P. C., & Plume, R., 2004, *ApJS*, 153, 523
- Lynds, B. T. 1962, *ApJS*, 7, 1
- Mouschovias, T. C. 1976, *ApJ*, 207, 141
- Myers, P. C. 2005, *ApJ*, 623, 280
- Myers, P. C., & Lazarian, A. 1998, *ApJ*, 507, L57
- Narayanan, G. 1997, PhD thesis, University of Arizona
- Narayanan, G., Moriarty-Schieven, G., Walker, C. K., & Butner, H. M. 2002, *ApJ*, 565, 319

- Narayanan, G., Walker, C. K., & Buckley, H. D. 1998, *ApJ*, 496, 292
- Ohashi, N., Lee, S. W., Wilner, D. J., & Hayashi, M. 1999, *ApJ*, 518, L41
- Shu, F. H. 1977, *ApJ*, 214, 488
- Stanimirovic, S., Staveley-Smith, L., Dickey, J. M., Sault, R. J., Snowden, S. L. 1999, *MNRAS*, 302, 417
- Tafalla, M., Myers, P. C., Caselli, P., Walmsley, C. M., & Comito, C. 2002, *ApJ*, 569, 815
- Tafalla, M., Mardones, D., Myers, P.C., Caselli, P., Bachiller, R., & Benson, P.J. 1998, *ApJ*, 504, 900
- Visser, A. E., Richer, J. S., & Chandler, C. J. 2002, *AJ*, 124, 2756
- Ward-Thompson, D., Motte, F., & Andre, P. 1999, *MNRAS*, 305, 143
- Walker, C. K., Narayanan, G., & Boss, A. P. 1994, *ApJ*, 431, 767
- Whitworth, A. P., & Ward-Thompson, D. 2001, *ApJ*, 547, 317
- Williams, J.P., Myers, P.C., Wilner, D.J., & Di Francesco, J. 1999, *ApJ*, 513, L61 (Paper I)
- Woody, D. P., et al. 2004, *Proc. SPIE*, 5498, 30

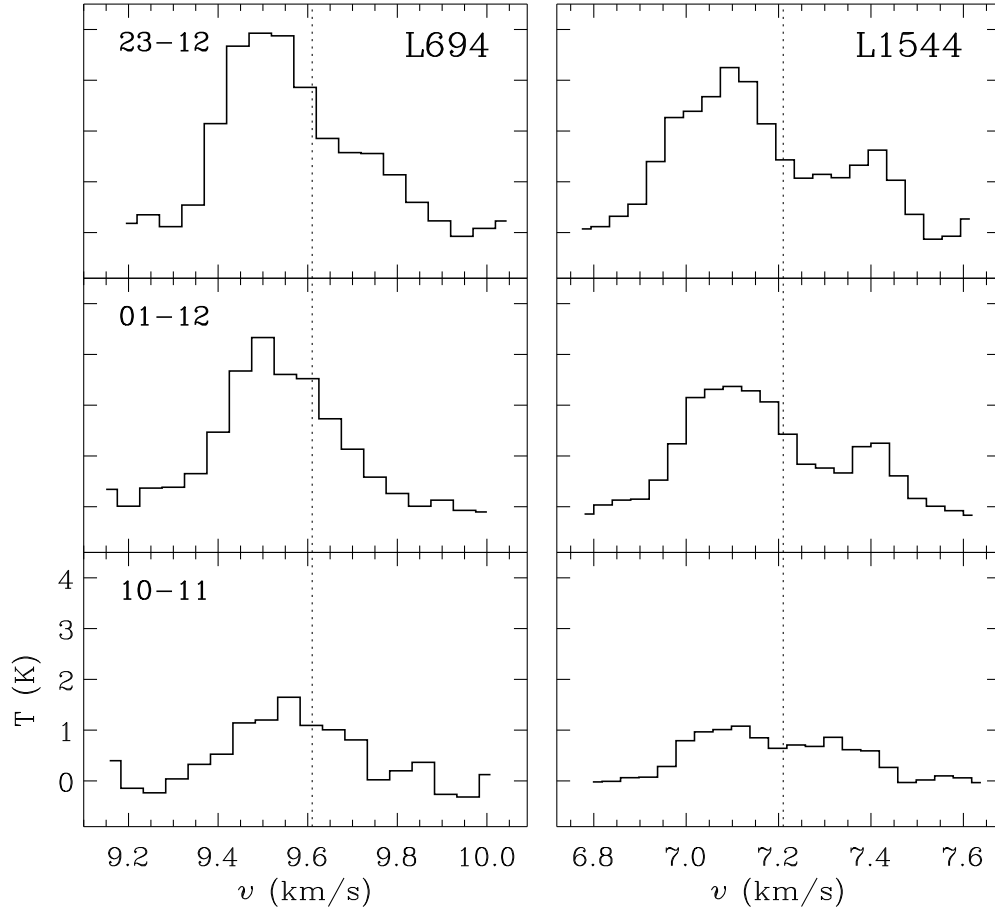


Figure 1: Comparison of $N_2H^+(1-0)$ spectra toward the centers of L694-2 and L1544 at the same linear resolution, 2300 AU. Three hyperfine components are shown, ordered from high to low optical depth, and the dotted line shows the systemic velocity for each core. The increasing asymmetry with opacity in each core is strong evidence for collapse.

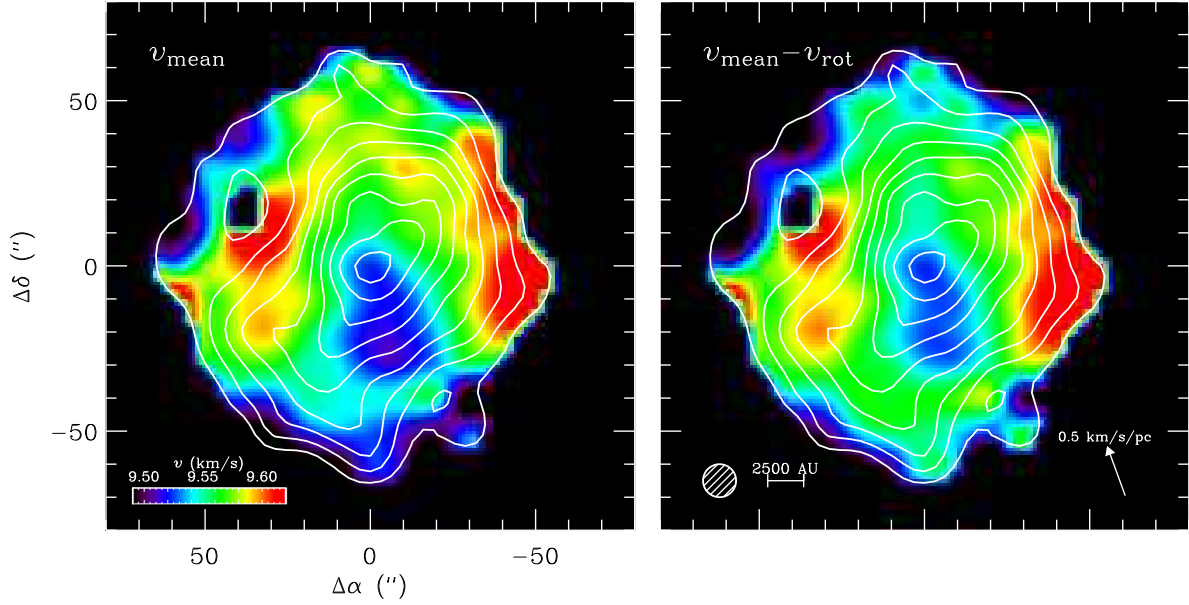


Figure 2: $\text{N}_2\text{H}^+ 1_{23} - 0_{12}$ intensity and velocity structure in L694-2. The left panel shows the mean velocity in colors overlaid on contours of integrated emission. The right panel shows the residual velocity field after subtracting a linear gradient due to core rotation. The direction and magnitude of the velocity gradient are shown in the lower right corner. The $10''$ resolution of the data and scale bar are shown in the lower left corner. The color scale ranges from 9.49 to 9.62 km s^{-1} and contours have starting point and increments of 0.12 K km s^{-1} in both panels.

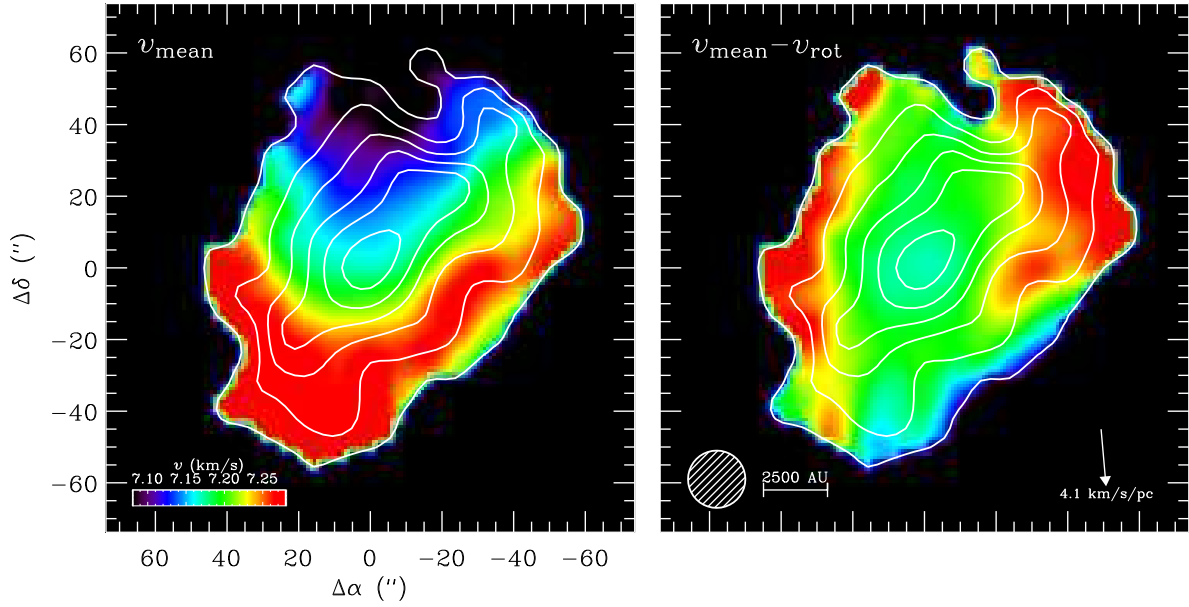


Figure 3: Similar plot as Figure 1 for L1544. The color scale ranges from 7.08 to 7.28 km s^{-1} and contours have starting point and increments of 0.16 K km s^{-1} in both panels. These plots were made with the data smoothed to the same linear resolution, 2300 AU, as the L694-2 data. Note that the velocity gradient is much higher in L1544 and the color scale is therefore stretched over a wider range. This has the effect of reducing the contrast of the central blue-bulge feature.

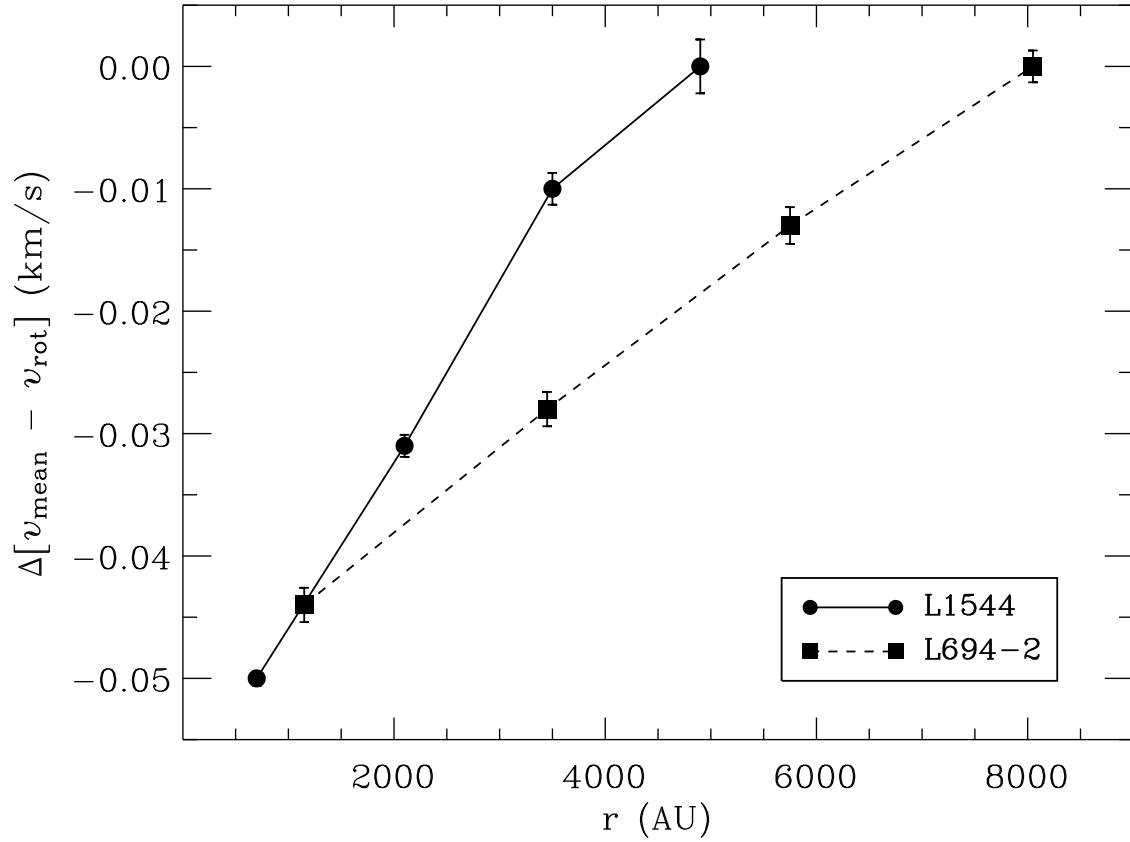


Figure 4: Comparison of the blue-bulge signature in L694-2 and L1544. Each point is a radial average in $10''$ annuli of the residual velocity field in the right panels of Figures 2 and 3. The velocity scale is set to zero at the outermost radii to show the blueward shift of mean velocity toward the center of each core. The errors are the standard deviation of the mean. The bluebulge is larger in extent but shallower in L694-2 (squares connected by a dashed line) compared to L1544 (circles connected by a solid line).

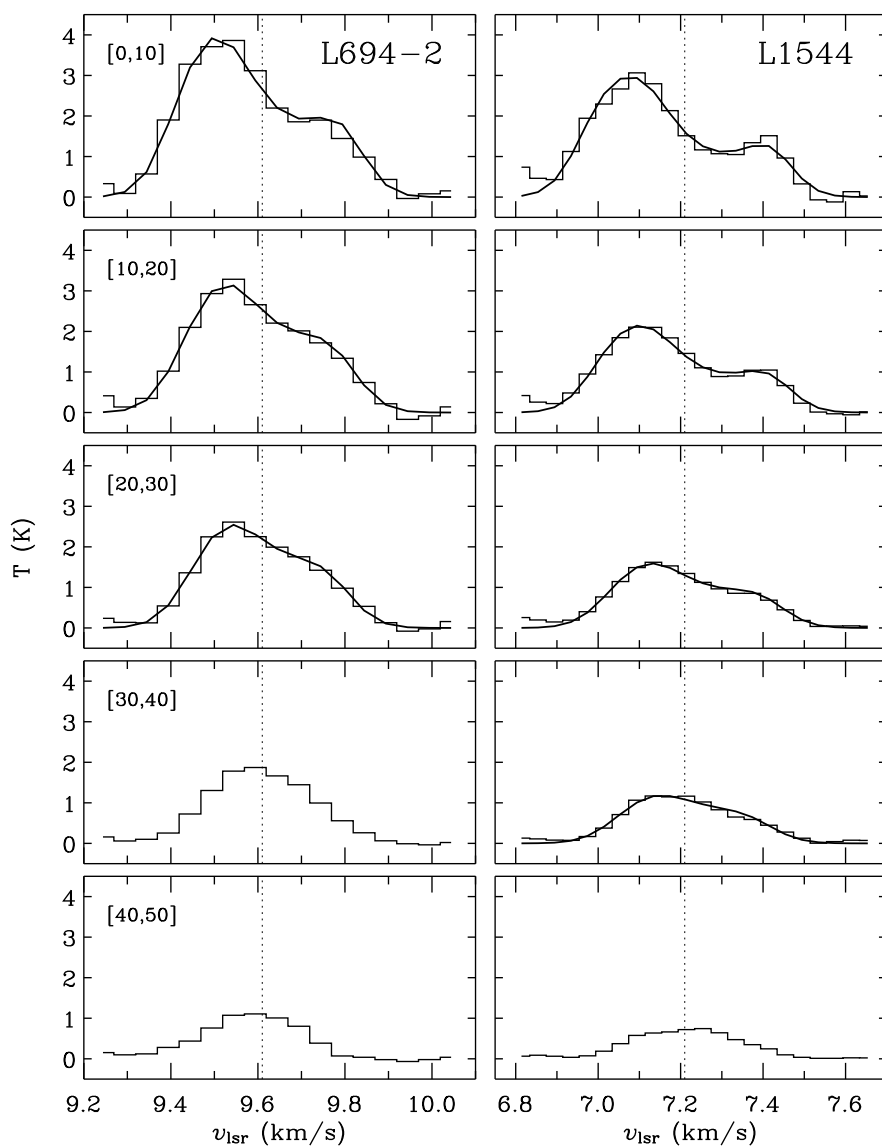


Figure 5: Radially averaged N_2H^+ $1_{23} - 0_{12}$ spectra (histogram) and two-layer model fits (line) for the two cores. L694-2 is on the left hand side, L1544 on the right. The averaging interval, in arcseconds, is shown in the top left hand corner of the left panel and is the same in the right panel. The vertical dotted line is the systemic velocity of each core. The shoulder like profile toward the center of L694-2 contrasts with the two distinct peaks toward the center of the more opaque L1544.

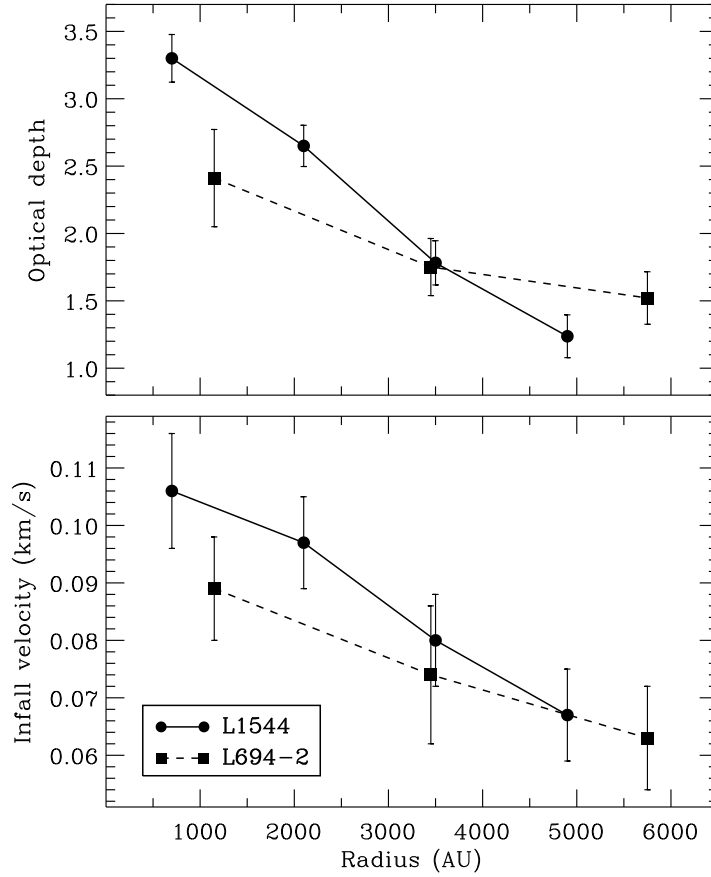


Figure 6: Optical depth and infall speed variation with radius, derived from the two-layer spectral fits. The errors were determined from multiple fits to fake spectra created by adding noise to the best fit models. L694-2 (squares connected by a dashed line) has a shallower opacity gradient and lower central values of opacity and infall speed than L1544 (circles connected by a solid line). This may reflect an earlier evolutionary state or a slightly lower mass.

TABLE 1
Two layer infall fit parameters

Annulus (")	v_{LSR} (km s ⁻¹)	σ (km s ⁻¹)	T_{peak} (K)	τ	v_{in} (km s ⁻¹)
L694-2					
0 – 10	9.61	0.078	9.3	2.4 ± 0.36	0.089 ± 0.009
10 – 20	9.61	0.081	8.9	1.8 ± 0.21	0.074 ± 0.012
20 – 30	9.61	0.081	8.0	1.5 ± 0.20	0.063 ± 0.009
L1544					
0 – 10	7.20	0.084	7.1	3.3 ± 0.18	0.106 ± 0.010
10 – 20	7.21	0.083	6.1	2.7 ± 0.15	0.097 ± 0.008
20 – 30	7.22	0.086	5.8	1.8 ± 0.16	0.080 ± 0.008
30 – 40	7.22	0.086	5.4	1.2 ± 0.16	0.067 ± 0.008